Fundamental research on the voltammetry of polycrystalline gold

Yang, S.


Murloc!
A captured big fish
Murloc*
*A monster with
a human body
and a fish head
一个简单误判引发的蝴蝶效应。
The butterfly effect triggered by
a simple misjudgment.

2

Redefinition of the active species and mechanism of the oxygen evolution reaction on gold oxide

Abstract

Accurately identifying the active species of catalytic materials and understanding how they catalyze the oxygen evolution reaction (OER) are critical for the development of energy storage technologies. In this contribution we identify two pH-dependent active oxides by mapping the reduction behavior of gold oxide and by in situ surface-enhanced Raman spectroscopy. It was found that α oxide# is preferentially formed in an acidic solution whereas β oxide, $Au(OH)_3$, is preferably formed in an alkaline solution. In line with the presence of two different surface structures on gold, there are two OER mechanisms: one wherein water splitting occurs via proton-coupled electron transfer (PCET) steps mediated by α oxide, and a mechanism wherein electron and proton transfer are decoupled, and is mediated by a deprotonated form of $Au(OH)_3$. This identification of pH-dependent oxides offers a different perspective in our understanding of the OER mechanism on metal oxides in a full pH scale range.

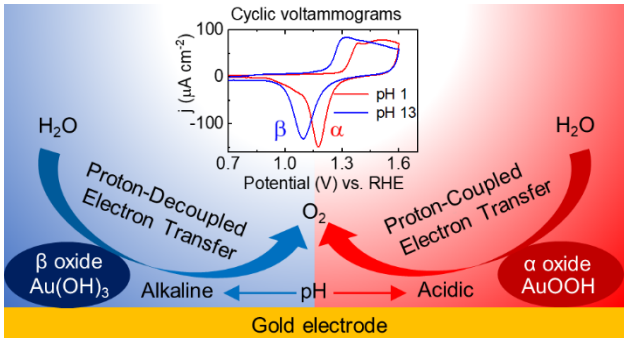

 # Note: In Chapter 2, we previously suggested that α oxide *could be AuOOH according to some literature. However, upon further examination, we've found that attributing AuOOH to α oxide is not reasonable, as it fails to account for various behaviors of α oxide. Consequently, we have reverted to the more conventional structure of gold oxide (Au_2O_3) in the subsequent chapters.*

This chapter was published as a research article: S. Yang, D. G. H. Hetterscheid*, *ACS Catal.* **10**, 12582-12589 (2020).

2.1 Introduction

More than two hundred and thirty years ago the first water electrolysis experiment was carried out by evolving hydrogen and oxygen separately at two gold electrodes.[1, 2] At present, water splitting is considered as an ideal solution to the world's renewable energy storage problem.[3-5] Using sunlight to split water into hydrogen and oxygen allows for the conversion of solar energy to chemical energy. This energy can be converted back to electricity in a fuel cell. It is widely accepted that one of the key bottlenecks in the overall water splitting reaction is the slow kinetics of the catalytic water oxidation reaction taking place at the anode.

Metal oxides are considered the best and most stable electrocatalysts for water oxidation.[3, 6, 7] In general oxidation mechanisms of noble metals involve three stages: (a) 2-dimensional (2D) electrodeposition of OH and O species on the metal surface; (b) quasi-3D surface reconstruction and place-exchange between the OH or O species and surface metal atoms; (c) growth or thickening of the oxide film.[8] Further development of the oxide film formation includes thin oxide films by stages (a) & (b) and thick hydrous oxide films by extension of oxide growth beyond the monolayer lavel.[9] Those mechanistic models are not only crucial for guiding catalyst design,[10, 11] but also for our understanding of the oxygen evolution reaction (OER) mechanism on metal oxides.[6, 12]

The initial quasi-3D metal oxide formation proceeding via reconstruction and place-exchange was identified not only on the basis of electrochemical behavior,[8, 13] but was also directly observed by atomic-resolution scanning tunneling microscopy and surface structure analyses.[14, 15] However, those in-situ observations and surface analysis techniques become less useful in the discussion of thicker oxide film formation, because these metal oxide layers are typically highly disordered.[16] Despite the lack of an effective detection of the surface structure of thicker oxide films, a concept of so-called hydrous oxide films involving thicker oxide formation was put forward on the basis of the observation that separate reduction peaks can be observed upon reduction of the metal oxide.[8, 9] In those reports the separation of the metal oxide reduction peaks was assumed to correspond to reduction of the inner-monolayer and the outer-hydrous layer of the metal oxide surfaces, respectively.

In this article we return to gold, the electrode material originally used two hundred and thirty years ago, and demonstrate that the model of inner and outer hydrous oxide films is incorrect. We identify that different active species, whose formations are pH dependent, play a role by combining the observed reduction behavior of gold oxide and in situ surface-enhanced Raman spectroscopy. Identification of this pH-dependent oxide is critical in order to fully understand the OER mechanism.

A typical and conventional OER mechanism on a metal oxide surface involves four proton-coupled electron transfer (PCET) steps at the oxide-electrolyte interface.[7, 17] The PCET-OER mechanism emphasizes the importance of optimizing the binding strength of reaction intermediates on surfaces to get high OER activities, which allows one to make OER activity predictions according to electronic structure parameters of the metal oxide.[4, 18] However the PCET-OER mechanism is not necessarily correct in all cases. OER activities that depend on the pH on the reversible hydrogen electrode (RHE) scale have been observed for various metal oxides in alkaline environment,[19-21] indicating that the OER process follows electron transfer steps that are not coupled to proton transfer on those metal oxides. The origin of pH-dependent OER mechanisms on the RHE scale has been revealed in recent years. For example, high-index facets of polycrystalline surfaces on oriented RuO_2 surfaces,[22] deprotonation of Ni-based catalysts,[23] and the covalence of metal-oxygen bonds in perovskites [21] can cause pH-dependent OER activity on the RHE scale. Moreover, many other explanations regarding OER mechanisms are only consistent in a relatively narrow pH range.[6, 21, 23] Although the difference in OER activity in acidic and alkaline solution is often related with the acid−base characteristics of the surface,[17, 24] lack of a clear explanation for these so-called “acid−base characteristics” limits our understanding of water splitting in a full pH range. In this manuscript we show that the mechanism wherein OER occurs on gold depends strongly on the surface structure of gold oxide, and that proton and electron transfer are coupled under acidic conditions, whereas these are decoupled during the OER at alkaline conditions.

2.2. Experimental section

2.2.1 General.

All glassware was thoroughly cleaned to remove impurities by overnight submersion in an aqueous 0.5 M H_2SO_4 solution mixing with 6.3 mM $KMnO_4$, followed by removal of excess $KMnO_4$ on the glassware in diluted H_2SO_4 and H_2O_2. The glassware was subsequently rinsed five times and boiled two times in Millipore MilliQ water (resistivity = 18.2 MΩ cm). Prior to electrochemical experiment, the glassware was boiled once in MilliQ water. Alumina suspensions (1.0, 0.3, and 0.05 μm) were obtained from Buehler. Electrolyte solutions were prepared with Suprapur® (Merck) reagents and MilliQ water. pH measurements were done using a Hanna Instruments HI 4222 pH meter which was calibrated using IUPAC standard buffers.

2.2.2. Electrochemical measurements.

All electrochemical measurements were conducted with an Autolab PGSTAT 12, 204 and 128N potentiostats in combination with Autolab NOVA software and carried out in conventional single compartment three-electrode glass cells at around 25 °C. A PEEK encapsulated gold electrode (A = 0.0314 cm^2, Metrohm) was used as working electrode, and a gold wire was the counter electrode, while a reversible hydrogen electrode (RHE) was employed as the reference electrode. Before every experiment the working electrode (the PEEK encapsulated gold) was manually polished for 2 minutes with 1.0, 0.3, and then 0.05 μm alumina suspensions on Buehler cloth polishing pads, followed by sonication in MilliQ water for 10 minutes. At the same time, the counter electrode (the gold wire) was flame annealed and rinsed with MilliQ water. The reference electrode (RHE) consisted of a Pt wire was connected via a Luggin capillary and continuously bubbled with H_2 gas during measuring.

The concentration of electrolyte solution was kept at 0.1 M for different pH solutions from pH 1-13 were obtained by mixing 0.1 M H_2SO_4, NaOH and Na_2SO_4. Unless stated otherwise, pH 1-13 represent solutions with fixed pH value comprising H_2SO_4, NaOH or Na_2SO_4 in this article. Dissolved oxygen in solution was removed prior to measurements by aeration with argon (purity grade 5.0) for at least 30 min. Argon was kept flowing above the solution during experiments. The onset potential of OER is acquired by intersection of tangents between the baseline and the rising current in the positive scan of Cyclic voltammograms, as shown in Fig.

S1.[25] Tafel analysis was done at steady state conditions and was used to understand OER reaction mechanism (see Fig. S10a&b).[26]

2.2.3 In situ surface enhanced Raman spectroscopy (SERS).

In situ surface enhanced Raman spectroscopy (SERS) was performed with a confocal Raman microscope (LabRamHR, Horiba Yobin Yvon) with an Olympus 50 × microscope objective, which was not immersed in the electrolyte, into a 5 μm spot on the electrode surface, which has been documented previously.[6, 27, 28] Backscattered light was filtered by a 633 nm edge filter, directed to the spectrograph and to the detector. With this configuration, a resolution of 1.2 cm^{-1} was obtained.[29] The electrochemical SERS experiments were made with an Ivium potentiostat/galvanostat (IviumStat). Figure S2 shows a schematic diagram of the electrochemical setup for in situ surface-enhanced Raman spectroscopic measurements. Each SERS was acquired with the accumulation of 100 scans with 1 s collection time.

A roughened gold surface was used as the working electrode. The working electrode was mechanically polished to a mirror finish using alumina with different grain size to 0.05 μm, rinsed with MilliQ water and sonicated for 15 min to remove all residuals of mechanical polishing. Then the gold electrode was electrochemically roughened by 25 oxidation-reduction cycles (ORC) in a 0.1M solution of KCl. The ORC were performed between -0.30 and 1.20 V vs. the saturated calomel electrode (SCE), which were held for 30 s and 1.3 s, respectively. A brownish surface was formed after roughening gold by this method.[6, 30] The quality of Au roughing can be visualized by a comparison of the current of the CV before and after Au roughing, as shown in Fig. S3. SERS spectra were recorded at 1 V vs RHE and set as the background signal and subtracted from further measurements in the same solution. Different backgrounds were set for solutions of different pH (H_2SO_4, Na_2SO_4, NaOH). All data were processed using Origin Pro 9.1.

2.3. Results and discussion

2.3.1 Inconsistencies in conventional models for the electrochemical redox behavior of gold.

In a typical cyclic voltammogram of gold (Fig.1a), the most notable oxide formation response in the positive sweep is an extended plateau rather than sharp peaks, independent of the applied pH. Formation of this plateau is attributed to the increased energy required to generate additional oxide by gradual changes in the hysteresis of the oxidation potential between Au and Au-OH species in the oxide layer.[31] It is therefore difficult to investigate the gold oxidation chemistry through this continuous oxidation process in the positive sweep. The behavior of gold in the negative sweep is more indicative of the processes taking place at its surface. Only one reduction peak can be detected in acidic solution, while the reduction peak splits into two separated peaks upon increasing the pH. Stable gold oxide with a +III oxidation state can be formed by the reaction ($2\mathrm{Au} + 3H_2\mathrm{O} \rightarrow Au_2O_3 + 6H^+ + 6e^-, E^O = 1.46\,V$), which is illustrated by the Pourbaix diagram of gold. Gold oxide with a +IV oxidation state can only be formed at a very high electric field by the reaction ($2\mathrm{Au} + 4H_2\mathrm{O} \rightarrow 2\mathrm{Au}O_2 + 8H^+ + 8e^-, E^O = 4.14\,V$).[32, 33] Consequently, Au(III) is the only oxidation state of gold present in the gold oxide layers as was shown by ex situ X-ray photoelectron spectroscopy (XPS)[34] and in situ extended X-ray absorption fine-structure (EXAFS) studies.[35] Because only one oxidation state (the trivalent) is involved, the presence of more than one reduction peak cannot be explained by different oxidation states of gold.

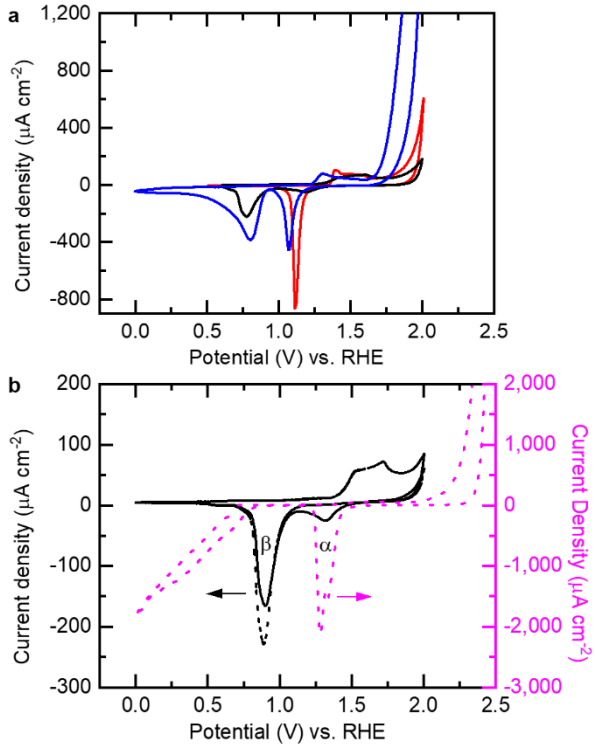

Figure 1. Electrochemical redox behavior of gold. **a**, Cyclic voltammograms (CVs) of gold between 0-2 V vs. RHE at 50 mV/s in Ar-saturated 0.1 M H_2SO_4 (red line), Na_2SO_4 (black line) and NaOH (blue line). **b**. CVs of gold vs. RHE in Ar-saturated 0.1 M Na_2SO_4 solution. Scan range of CVs: 0-2 V (black line); 0-2.7 V (pink dotted line); Black dotted line: gold was first oxidized between 1.6-1.8 V vs. RHE for 200 s, prior to recording the CV between 0-2 V vs. RHE in fresh 0.1 M Na_2SO_4 solution.

On the basis of the "separated reduction peaks" that can be observed for gold, the concept of hydrous oxide films was put forward last century.[9, 36, 37] The two main gold oxide reduction peaks have historically been assigned to a compact inner monolayer oxide and a hydrous outer layer oxide. In acidic solution the hydrous outer oxide layer was suggested to be thin enough so that its reduction peak overlaps with the reduction peak of compact inner oxides. At higher pH the thicker hydrous outer oxide layer was proposed to cause the reduction peak to split into two peaks (Fig. 1a).[31] The trivalent oxidation state of gold in all oxide forms has been regarded as consistent with the inner- and outer-layer oxide model.

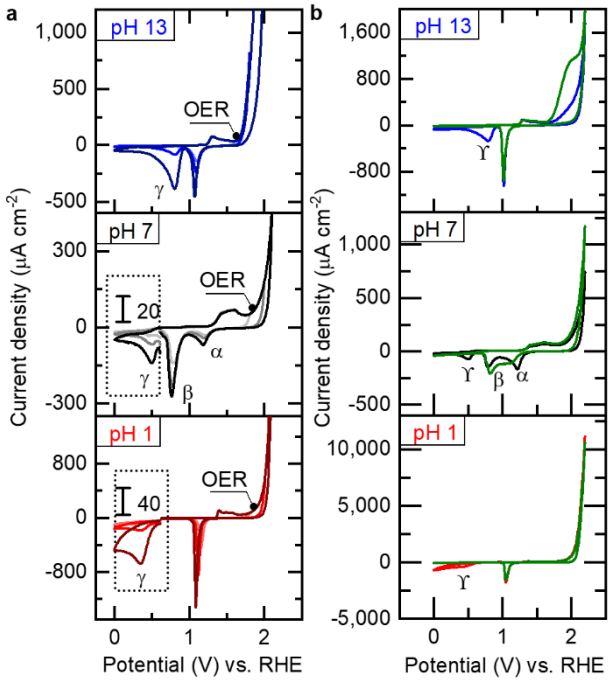

Figure 2. Recognition of the γ peak being associated with oxygen reduction. **a**, Cyclic voltammograms (CVs) of gold vs. RHE at 50 mV/s with change of scan range in Ar-saturated solution; The γ peaks are amplified (by different multiples) to clearly show their position; **b**, CVs on a gold rotating disk electrode (RDE) at 0 rpm between 0-2.2 V vs. RHE in Ar-saturated pH 1 (red line), pH 7 (black line), and pH 13 (blue line). Green line: CVs of RDE with 3000 rpm at those different pH solutions.

However, there are major problems with the inner- and outer-hydrous oxide model. In a CV of gold at neutral pH (Black line in Fig.1b), the relatively positive reduction peak corresponds to the inner monolayer of oxide, named as α oxide, and another relatively negative reduction peak is assigned to the outer hydrous oxide, named as β oxide. According to the mechanism of hydrous oxide film formation, the α peak cannot disappear because it represents the inner structure of the oxide layers. However, only the β peak, i.e. no α peak, can be detected on an oxidized gold electrode, which is oxidized at 1.6-1.8 V vs. RHE in advance (Black dotted line in Fig.1b). Moreover, when the upper limit of the positive scan is extended from 2.0 to 2.7 V (Pink dotted line Fig. 1b) the α peak increases to a huge reduction peak; this is not at all in

line with the hydrous oxide film model, where the α peak should not change in magnitude because it supposed to correspond to an inner monolayer.

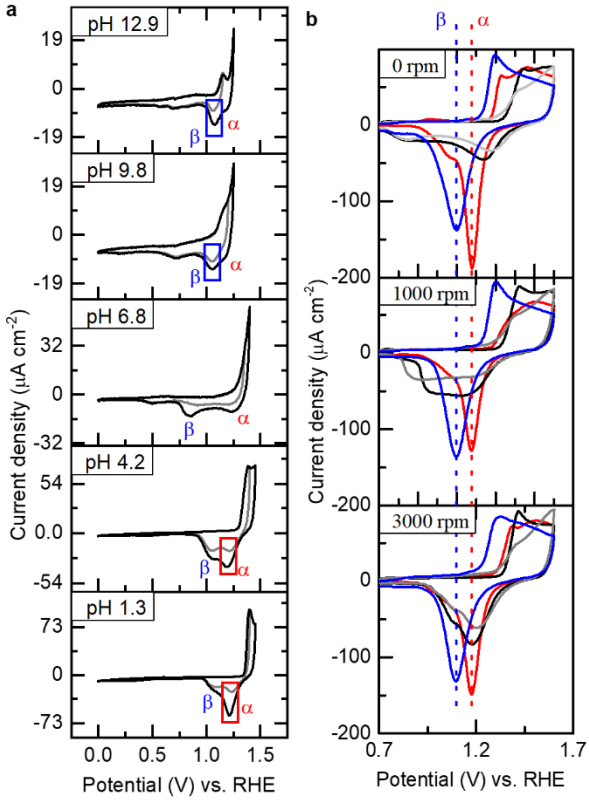

Figure 3. Identification of active gold oxides. **a**, Cyclic voltammograms (CVs) of gold in different Ar-saturated pH solutions at 50 mV/s. The upper limit of CV is kept to the range of potentials where gold oxidation occurs. **b**, CVs of of gold (RDE) between 0-1.6 V vs. RHE at rotation rates with different Ar-saturated 0.1 M electrolytes: H_2SO_4 (red line), Na_2SO_4 (black line), $NaClO_4$ (grey line), NaOH (blue line). The exact change of the potential value as a function of the rotation speed is shown in Fig. S4.

Figure 2a shows the change of CVs for gold with the increase of the upper vertex potential in acidic, neutral and alkaline solution. A new reduction peak appears once the upper limit of the voltammetry experiment was set above the onset potential of the oxygen evolution reaction (OER). In order to further identify the γ peak, the electrochemistry of gold was recorded in acidic, neutral and alkaline solution with a rotating disk electrode (RDE), as shown in Fig. 2b. It is clearly shown that the γ peak disappears upon rotation, while the reduction peaks of gold

oxide do not significantly change once O_2 is removed at a high rotation rate. This implies that the γ peak is the result of reduction of O_2. Note that the γ peak in alkaline solutions is often misinterpreted as a β peak of gold oxide reduction in the literature,[31, 37, 38] which makes the discussion of the redox chemistry of gold much more complex.

In order to eliminate the interference of O_2, CVs of gold were measured as a function of pH by keeping the upper limit of CV at the potentials at which gold oxidation begins while still below the onset potential of OER (Fig.3a). Both the α and β peaks were detected in all solutions irrespective of the pH. The CVs in alkaline solution revealed that β oxide is formed first while the applied potential is kept well below the reduction potential of α oxide; this is contrary to the past hydrous oxides films model wherein the inner α oxide must form first. Furthermore, a larger α peak was found in an acidic solution, while the β peak was significantly larger under alkaline conditions. This implies that α and β oxides are two relatively independent forms of gold oxide, whose formation is dependent on the pH. A similar result is obtained when the solution was changed from a Na_2SO_4 solution to a $NaClO_4$ solution, which means there is little influence of the electrolyte (Fig. S5).

2.3.2 Redefinition of the active gold oxides.

The initial stage of gold oxidation has been extensively discussed in the past.[8, 13] Hydroxide ion under alkaline conditions and water under acidic conditions, first chemisorb on gold to form Au-OH_{ads}. The Au-OH_{ads} would continue to convert to $Au(OH)_3$ by place exchange reactions between Au and OH^-. The initial gold oxide $Au(OH)_3$ formation is in good agreement with DFT-based computational studies of the surface thermodynamics of electrochemistry of gold.[6] Since $Au(OH)_3$ relies on place exchange reactions between Au and OH^-, $Au(OH)_3$ formation should be enhanced with increasing the pH. From a comparison of CVs at different pH (Fig. 3a), the β peak therefore most likely corresponds to reduction of $Au(OH)_3$. Actually, gold(III) precipitations in alkaline media have been shown to correspond to $Au(OH)_3$ but not $Au_2O_3{\cdot}nH_2O$ according to XRD, TEM, Au Mössbauer spectroscopy, X-ray absorption spectroscopy (XAS) and thermogravimetry /differential thermal analysis (TGA/DTA) studies.[39]

It is interesting to note that the reduction potential difference of α and β oxide is roughly 0.13 ± 0.01 V in both acid and alkaline solutions, but becomes more than 0.4 V in neutral conditions (0.42V at pH 6.8). Therefore RDE experiments were conducted with varying rotation rates (Fig. 3b). At 0 rpm there is a minor positive shift of the α potential and a clear negative shift of the β peak in neutral solution compared to both acidic and alkaline media, irrespective of whether Na_2SO_4 or $NaClO_4$ was used as an electrolyte. The potential shifts of the α and β peaks in neutral media can be avoided upon increasing the rotation rates of the gold electrode. At 3000 rpm, it is clearly shown that the peak positions of α and β oxide in neutral solution coincide with the peak position of α in acid and the position of β in base. An effect of the scan rate on the peak position of the reduction peaks was investigated (Fig. S6). Both oxide reduction peaks show only a minor negative potential shift with increase of the scan rate. Their currents are linearly dependent on the scan rate, which is fully consistent with the characteristics of an irreversible oxide reduction process on the gold surface.

In situ surface enhanced Raman spectroscopy (SERS) was measured to further identify the structure of α and β oxide. The potential-dependent vibrational spectra in 0.1 M H_2SO_4, Na_2SO_4 and NaOH solution are shown in Fig. 4b-d. The observed broad frequency bands at 530-565 cm^{-1} are characteristic of the ν(Au-O) vibration, which can be detected when the applied potential is set above 1.35 V in H_2SO_4 1.45 V in Na_2SO_4, and 1.2 V in NaOH., These oxidation potentials are also consistent with the potential where gold oxidation occurs in LSV measurements (Fig. 4a). The ν(Au-O) vibration may point to oxide formation, though the band is especially broad and its frequency is easily influenced, by e.g. absorption of the electrolyte.

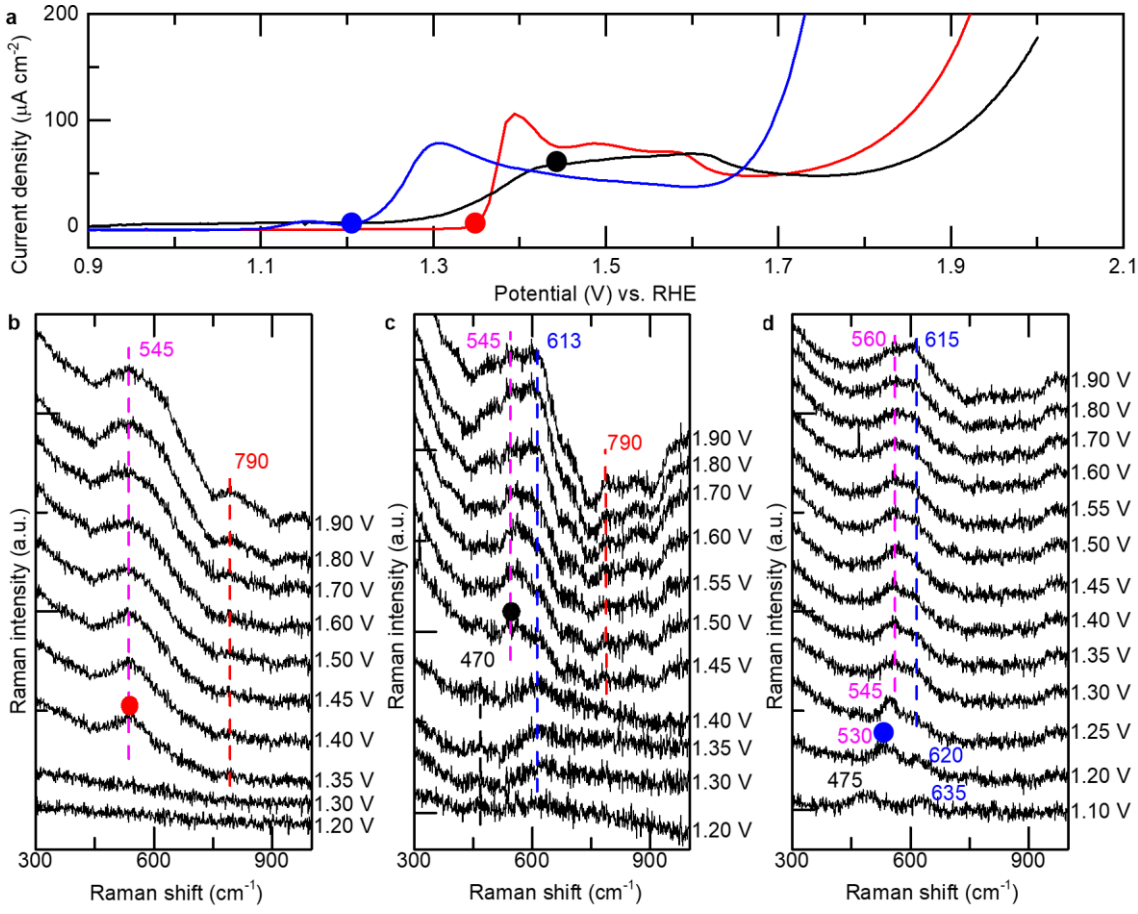

Figure 4. In situ Surface Enhanced Raman Spectroscopy (SERS) of gold oxidation. **a**, Linear sweep voltammetry (LSV) for electrocatalytic water oxidation from 0.9 V to 2 V vs. RHE at 50 mV/s on gold electrode in Ar saturated 0.1 M H_2SO_4 (red line), Na_2SO_4 (black line) and NaOH (blue line) solution. **b-d**, SERS of gold oxidation in 0.1 M H_2SO_4 (b), Na_2SO_4 (c) and NaOH (d), respectively. Oxidation potentials were recorded on the RHE scale. Solid circles represent the points where the ν(Au-O) vibration becomes visible in 0.1 M H_2SO_4 (red circle), Na_2SO_4 (black circle) and NaOH (blue circle) solutions.(Fig. S7), and/or the applied potential.[40] The wide Raman bands are most likely due to different coordination geometries and hydration states of the gold surface.[41]

The normal surface electro-oxidation of noble metals includes two steps: (i) initial deposition of O or OH species; (ii) ”oxide film” formation by place exchange with the surface metal atoms and adsorbed oxygen species along with further electron transfer.[8] These two steps

cannot be clear-cut distinguished. A band around 470-475 cm^{-1} is assigned to the reversible adsorbed OH^- (Fig. 4c-d). The ν(Au-OH^-) occurs around 400-450 cm^{-1} in 1 M KOH according to literature and shifts to higher frequencies at more positive potentials.[41] A significant frequency change from ν(Au-OH^-) at 475 cm^{-1} at 1.1 V to higher ν(Au-O), 530-560 cm^{-1}, with more positive potential in NaOH indicates a change in the oxide formation process from step (i) to step (ii). This is explained by yielding a strong ionic component to the Au-O bond energy in the process of place exchange between gold and oxygen since these gold atoms would get a more positive formal oxidation state.[41] According to the Raman spectrum of bulk-phase solid $Au(OH)_3$, the ν(Au-OH) vibration of $Au(OH)_3$ should be observed at 635 cm^{-1}.[41] Interestingly, the ν(Au-OH) vibration of $Au(OH)_3$ at 635 cm^{-1} first occurs at 1.1 V in NaOH and has a minor shift to 613 cm^{-1} with higher oxidation potentials (Fig. 4d). Note that ν(Au-OH) vibration at 613 cm^{-1} also can be observed in a Na_2SO_4 solution (Fig. 4c). This is consistent with the occurrence of the β peak in CVs of gold (Fig.3) caused by the reduction of $Au(OH)_3$.

In addition, the absence of an α peak in the CV in an NaOH solution (Fig.3a) is fully in line with the absence of a signal around 800 cm^{-1} in SERS experiments (Fig. 4d). Therefore, we assume the Raman signals recorded at approximately 820 cm^{-1} in perchloric media and at 790 cm^{-1} in sulfuric media is related to α oxide (Figure S7).

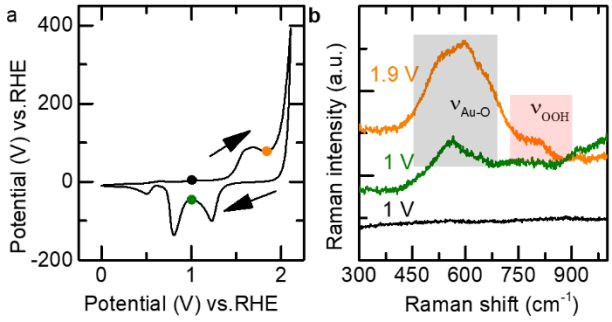

Figure 5 Reversibility of SERS of gold oxidation in 0.1 M Na_2SO_4. **a**, CV of gold electrode at 50 mV/s. **b**, SERS of gold oxidation in a positive scan and negative scan of CV.

In previous studies this band was found at values between 810 and 827 cm^{-1} in perchloric media.[6, 40, 42] A minor shift of 3-4 cm^{-1} was observed upon substitution of H_2O for D_2O.[40, 42] A significant shift of 74-77 cm^{-1} was observed upon substitution of $H_2{}^{16}O$ for $H_2{}^{18}O$ in previous

isotope studies.[6] Furthermore, the assignment of bands around 820 cm^{-1} to other forms of oxygen associated with Au (e.g. superoxo, oxo, and hydroxy) was excluded based on a series of DFT calculation.[27, 42] Therefore the signals in the range of 810 ± 20 cm^{-1} must be assigned to O-OH stretching. The O-OH stretching appears simultaneously with the appearance of ν(Au-O) of gold oxide in a H_2O_2 decomposition experiment on gold nanoparticles.[42] Tian and co-workers therefore claimed that the peak around 800 cm^{-1} must be assigned to an O-O stretch of an H-containing reaction intermediate, and not simply to an O-O stretch of peroxide. Interestingly two independent research groups (Bell and Koper) have claimed that the vibrational signal around 800 cm^{-1} was observed at least 0.4 V less positive than the onset of water oxidation in their in situ SERS experiments.[6, 40] However, according to DFT calculations of *OOH on gold and other metal oxides surface, the *OOH intermediate is the highest energy intermediate and should rapidly decompose into O_2.[7, 43] An explanation is that peroxidic species may exist within the oxide layer in acidic solution, which probably somehow related to a highly non-ordered structure.[19] However this still cannot explain the lack of an *OOH SERS signal in a low oxidation potential range at alkaline solution. Thus far these Raman signals have not been investigated in a full pH range. Koper and co-workers have put forward a more stable oxyhydroxide (AuOOH) formation mechanism in acidic solution on basis of DFT calculations. The oxyhydroxide is proposed an important role in the OER process. We therefore do consider the possibility that α oxide may predominantly be an oxyhydroxide, which structure may include *OOH species within oxide layer. In order to further confirm the relationship between α oxide and ν(OOH), an in situ SERS reversibility experiment was carried out in neutral solution (Fig. 5), where the collection time of SERS signals were increased from 1 second to 10 seconds to trace the change of SERS. Here, ν(Au-O) in the range of 500-620 cm^{-1} and ν(OOH) at 790 cm^{-1} can be detected once increase potential from 1 V to 1.9 V. When the potential is decreased from 1.9 V to 1 V the ν(OOH) will disappear, while some of the ν(Au-O) signal remains. At this potential of 1 V only β oxide can exist while α oxide is reduced. This confirms that the signal around 800 cm^{-1} does not simply represent surface-bound hydroperoxide species as an intermediate of OER, yet somehow must be related to the existence of α oxide .

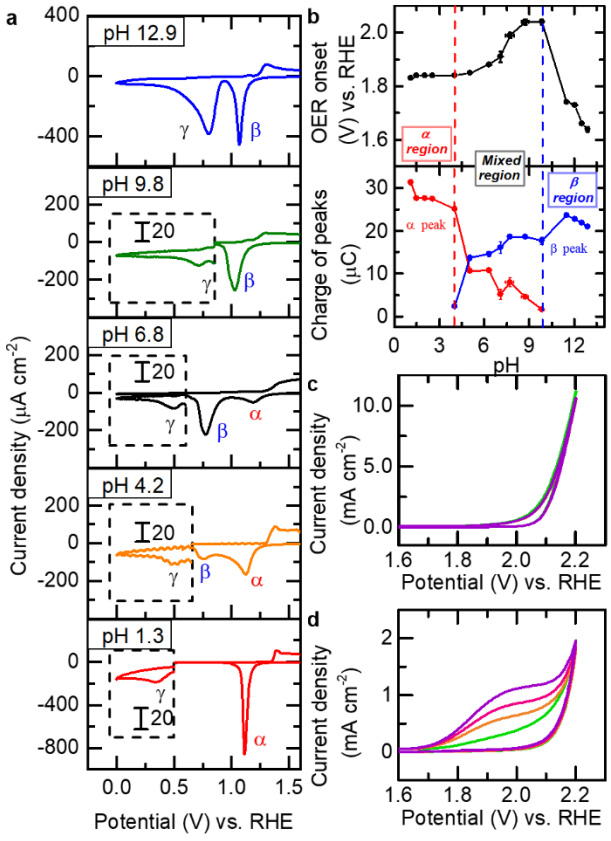

Figure 6. pH-dependent oxide formation and OER activity on gold. **a**, CVs of gold electrode showing the reduction peaks at 50 mV/s in different Ar-saturated pH solutions. Note that the scan range is 0-2V vs. RHE. The γ peaks are amplified (by different multiples) to clearly show their position. The oxidative areas in the 1.5-2 V range of these CVs, showing the OER, are shown in Fig. S8. **b**, The onset potential of OER (top) and the integrated charges of the α and β oxide reduction peaks at 50 mV/s in Ar-saturated solutions is plotted as a function of pH. The error bars represent the standard deviation of three measurements. **c-d**, CVs of gold (RDE) at 50 mV/s in Ar-saturated 0.1 M H_2SO_4 (c) or NaOH (d) solution at different rotation rates: 0 rpm (green line); 100 rpm (orange line); 1000 rpm (pink line) ; 3000 rpm (violet line); scan range is 0-2.2 V vs. RHE.

2.3.3 Two OER mechanisms leaded by two gold oxides.

Our results show that the structure of gold oxide is strongly dependent on the pH of the solution: α oxide, is preferentially formed in an acidic solution; β oxide, $Au(OH)_3$, is

preferentially formed in an alkaline solution (Fig. 6a). As with the surface structure of gold oxide, the mechanism of OER is also affected by the solution pH. The OER activity increases with decreasing pH in the low-pH region and with increasing pH in the high-pH region (Fig. S8). Very similar results have been obtained by Stahl and coworkers who revealed that different cobalt based active species exist at different pH values and have investigated the OER mechanism in a full pH region.[26] Although such pH dependent species may exist on more metal based catalysts, the lack of a clear understanding of the mechanism of pH dependent active species limits the development of better OER catalysts in case of several more metal based systems.

Figure 6b shows the OER onset potential and the integrated charges of the α and β oxide reduction peaks in a full pH window. The pH environment can be divided into three different regions: 1) The α region (pH lower than 4) in acidic solution; 2) The mixed region (pH from 4 to 10) in neutral solution; and 3) The β region (pH higher than 10) in alkaline solution. In the α region, α oxide is the only oxide that can exist in a stable form. In this window the OER onset potential is fixed at 1.84 V vs. RHE. This pH-independent OER activity on the RHE scale in the α region implies that the OER process at α oxide proceeds via four proton-coupled electron transfer (PCET) steps. In the mixed region, both α oxide and β oxide exist on the electrode surface. The amount of the two oxides changes with the pH of the solution in this region. The amount of α oxide decreases while the amount of β oxide increase with the increase of the pH. Interestingly, the OER onset potential also increases with pH. This shows that β oxide is less active for the OER than α oxide in this pH window. The OER activity level therefore strongly relies on the existence of α oxide in this mixed oxide region. In the β region at high pH values, only β oxide is present at the electrode surface. In this pH window the OER onset potential gradually decrease with an increase of the pH. This means that the OER must be pH dependent when catalyzed by β oxide, which implies that some of the proton and electron transfer steps are decoupled in the OER process in the high pH region For a reaction, the proton transfer step (PT) and electron transfer step (ET) will decouple if one of their activation energies is smaller than the activation energy of the PCET process.[17].

In order further evaluate the relationship between OER activity and the existence of oxides, a series of Tafel plots are obtained for these different pH regimes (Fig. S9, Table S1) In the α region, all Tafel plots overlap with Tafel slopes that are around 120 mV/decade. This further confirms that OER at α oxide proceeds via a pH independent process. In the mixed region the Tafel slopes are up to around 160-190 mV/decade, which is in agreement with a lower OER activity in this pH window. However the Tafel plots of β oxide appear initially at different potential regions and show that the evolution of oxygen starts earlier once the solution pH increases in β region. This is fully in line with a pH dependent OER process. Moreover, lower Tafel slopes (60-70 mV/decade) are found in the β region, which implies the decoupled OER process has a higher efficiency for oxygen evolution compared to the PCET OER process on α oxide.

The effect of solution pH on the proton affinity and electron affinity of the catalyst or reactant has been discussed during recent years.[17, 19, 44] According to acid-base characteristics of a catalyst on the surface, some catalysts have a proton affinity, which is equal to the (surface) pK_a of acid dissociation constant. If a solution pH is higher than the (surface) pK_a of a catalyst, deprotonation can occur to form a negatively charged surface leading to a decoupled electron-proton process, as shown in Fig.7. A very similar deprotonation process was observed recently in case of the water oxidation reaction at n-$SrTiO_3$.[45]

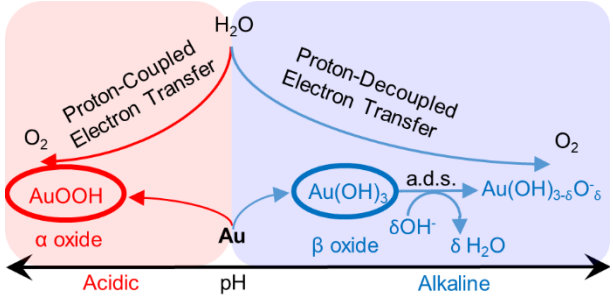

Figure 7. Proposed mechanism for electrocatalytic water oxidation on gold. In high pH region, the rate-limited step of oxygen evolution is deprotonation of $Au(OH)_3$ involving a decoupled proton transfer step.

This concept of surface deprotonation has been confirmed by thermodynamic explanations,[17] simple kinetic models,[46] and experiments.[19, 23] β oxide-$Au(OH)_3$ is also called

auric acid, and with a formula of H_3AuO_3, it is easy to speculate the existence of the (surface) pK_a of $Au(OH)_3$. Here, we do consider the influence of the acid-base characteristics of $Au(OH)_3$ ($Au(OH)_3 + \sigma OH^- \rightleftharpoons Au(OH)_{3-\sigma}O_\sigma^- + \sigma H_2O$) to the OER process in a high pH region.

The deprotonation process of β oxide can be illustrated by rotating disk experiments (Fig. 6c-d): showing no significant changes in the OER activity at pH 1 (Fig. 6c), while the OER activity in pH 13 massively increases with an increase of the rotation rate (Fig. 6d). This indicates that the mass transport of OH^- is not a determining factor for the PCET-OER process at α oxide, but is rate limiting for the uncoupled OER process on β oxide. Note that OH^- will likely act as a proton accepter in the deprotonation process occurring at β oxide, which explains why mass transport of OH^- is part of the rate determining step in the proton-decoupled electron transfer process. However, we cannot rule out that part of our observations are due to hydroxide becoming a substrate instead of water at the more alkaline conditions.[47, 48]

2.4. Conclusions

In summary, we have reassigned the α and β reduction peaks of gold to two independent oxides on the basis of our electrochemical and in situ Raman data. It was found that α oxide is preferentially formed in in a low-pH region, and β oxide-$Au(OH)_3$ in a high-pH region. Our studies further revealed that there are two OER mechanisms taking place on a gold oxide surfaces: i.e., water splitting to O_2 through proton-coupled electron transfer (PCET) steps on α oxide; and via a path wherein proton and electron transfer are decoupled on β oxide-$Au(OH)_3$. We believe that our findings are not restricted to gold, and offer different insights in how OER occurs at metal oxides.

2.5 Associated content

Supporting information.

Figures S1-S9 and Table S1 are included in the supporting information. This material is available free of charge via the Internet at http://pubs.acs.org.

2.6 Acknowledgments

This work was supported from the China Scholarship Council (award number 201706420073).

2.7 References

1. Paets van Troostwijk, A.; Deiman, J. R., *Ann. Phys.* **1790,** *2*, 130-141.
2. De Levie, R., *J. Electroanal. Chem.* **1999,** *476* (1), 92-93.
3. McCrory, C. C.; Jung, S.; Peters, J. C.; Jaramillo, T. F., *J. Am. Chem. Soc.* **2013,** *135* (45), 16977-87.
4. Suntivich, J.; May, K. J.; Gasteiger, H. A.; Goodenough, J. B.; Shao-Horn, Y., *Science* **2011,** *334* (6061), 1383-1385.
5. Browne, M. P.; Sofer, Z.; Pumera, M., *En. Envir. Sci.* **2019,** *12* (1), 41-58.
6. Diaz-Morales, O.; Calle-Vallejo, F.; de Munck, C.; Koper, M. T. M., *Chem. Sci.* **2013,** *4* (6), 2334-2343.
7. Rossmeisl, J.; Qu, Z. W.; Zhu, H.; Kroes, G. J.; Nørskov, J. K., *J. Electroanal. Chem.* **2007,** *607* (1-2), 83-89.
8. Conway, B. E., *Prog. Surf. Sci.* **1995,** *49* (4), 331-452.
9. Burke, L. D.; Lyons, M. E. G., Electrochemistry of Hydrous Oxide Films. In *Modern Aspects of Electrochemistry* White, R. E.; Bockris, J. O. M.; Conway, B. E., Eds. Springer: New York, 1986 Vol. 18, pp 169-189.
10. Bond, G. C.; Thompson, D. T., *Catal. Rev.* **1999,** *41* (3-4), 319-388.
11. Haruta, M., *Chemphyschem* **2007,** *8* (13), 1911-3.
12. Juodkazis, K.; Juodkazytė, J.; Juodienė, T.; Šukienė, V.; Savickaja, I., *Electrochim. Acta* **2006,** *51* (27), 6159-6164.
13. Tremiliosi-Filho, G.; Dall'Antonia, L. H.; Jerkiewicz, G., *J. Electroanal. Chem.* **2005,** *578* (1), 1-8.
14. Gao, X.; Hamelin, A.; Weaver, M. J., *Phys. Rev. B* **1991,** *44* (19), 10983-10986.
15. Lipkowski, J.; Ross, P. N., *Structure of Electrified Interfaces*. Wiley-VCH: New York, 1993; Vol. 2.
16. Weiher, N. Combined in situ and ex situ studies of an electrochemical interface: investigation of anodic oxide layers on gold. Freie Universitaet, Berlin, 2003.
17. Koper, M. T. M., *Chem. Sci.* **2013,** *4* (7), 2710-2723.
18. Frydendal, R.; Busch, M.; Halck, N. B.; Paoli, E. A.; Krtil, P.; Chorkendorff, I.; Rossmeisl, J., *ChemCatChem* **2015,** *7* (1), 149-154.
19. Diaz-Morales, O.; Ferrus-Suspedra, D.; Koper, M. T. M., *Chem. Sci.* **2016,** *7* (4), 2639-2645.
20. Giordano, L.; Han, B.; Risch, M.; Hong, W. T.; Rao, R. R.; Stoerzinger, K. A.; Shao-Horn, Y., *Catal. Today* **2016,** *262*, 2-10.
21. Grimaud, A.; Diaz-Morales, O.; Han, B.; Hong, W. T.; Lee, Y. L.; Giordano, L.; Stoerzinger, K. A.; Koper, M. T. M.; Shao-Horn, Y., *Nat. Chem.* **2017,** *9* (5), 457-465.
22. Stoerzinger, K. A.; Rao, R. R.; Wang, X. R.; Hong, W. T.; Rouleau, C. M.; Shao-Horn, Y., *Chem* **2017,** *2* (5), 668-675.
23. Trzesniewski, B. J.; Diaz-Morales, O.; Vermaas, D. A.; Longo, A.; Bras, W.; Koper, M. T.; Smith, W. A., *J. Am. Chem. Soc.* **2015,** *137* (48), 15112-21.
24. Kuo, D. Y.; Kawasaki, J. K.; Nelson, J. N.; Kloppenburg, J.; Hautier, G.; Shen, K. M.; Schlom, D. G.; Suntivich, J., *J. Am. Chem. Soc.* **2017,** *139* (9), 3473-3479.
25. Huang, Z.-F.; Wang, J.; Peng, Y.; Jung, C.-Y.; Fisher, A.; Wang, X., *Adv. Energy Mater.* **2017,** *7* (23).
26. Gerken, J. B.; McAlpin, J. G.; Chen, J. Y.; Rigsby, M. L.; Casey, W. H.; Britt, R. D.; Stahl, S. S., *J. Am. Chem. Soc.* **2011,** *133* (36), 14431-42.
27. Diaz-Morales, O.; Hersbach, T. J. P.; Hetterscheid, D. G. H.; Reek, J. N. H.; Koper, M. T. M., *J. Am. Chem. Soc.* **2014,** *136* (29), 10432-10439.
28. de Ruiter, J. M.; Purchase, R. L.; Monti, A.; van der Ham, C. J. M.; Gullo, M. P.; Joya, K. S.; D'Angelantonio, M.; Barbieri, A.; Hetterscheid, D. G. H.; de Groot, H. J. M.; Buda, F., *ACS Catal.* **2016,** *6* (11), 7340-7349.
29. Lai, S. C. S.; Kleyn, S. E. F.; Rosca, V.; Koper, M. T. M., *J. Phys. Chem. C* **2008,** *112* (48), 19080-19087.
30. Gao, P.; Gosztola, D.; Leung, L. W. H.; Weaver, M. J., *J. Electroanal. Chem.* **1987,** *233* (1-2), 211-222.
31. Burke, L. D.; Nugent, P. F., *Gold Bull.* **1997,** *30* (2), 43-53.
32. Pourbaix, M., *Atlas of Electrochemical Euilibria in Aueous Solution*. National Association of Corrosion Engineers: Houston, TX, 1974; Vol. 2nd edn, p 644.
33. Burke, L. D.; Buckley, D. T.; Morrissey, J. A., *Analyst* **1994,** *119* (5), 841-845.
34. Peuckert, M.; Coenen, F. P.; Bonzel, H. P., *Surf. Sci.* **1984,** *141* (2-3), 515-532.
35. Weiher, N.; Willneff, E. A.; Figulla-Kroschel, C.; Jansen, M.; Schroeder, S. L. M., *Solid State Commun.* **2003,** *125* (6), 317-322.
36. Lohrengel, M. M.; Schultze, J. W., *Electrochim. Acta* **1976,** *21* (11), 957-965.
37. Burke, L. D.; McRann, M., *J. Electroanal. Chem. Interf. Electrochem.* **1981,** *125* (2), 387-399.
38. Doyle, R. L.; Lyons, M. E. G., *J. Solid State Electrochem.* **2014,** *18* (12), 3271-3286.
39. Kawamoto, D.; Ando, H.; Ohashi, H.; Kobayashi, Y.; Honma, T.; Ishida, T.; Tokunaga, M.; Okaue, Y.; Utsunomiya, S.; Yokoyama, T., *Bull. Chem. Soc. Jpn.* **2016,** *89* (11), 1385-1390.
40. Yeo, B. S.; Klaus, S. L.; Ross, P. N.; Mathies, R. A.; Bell, A. T., *Chemphyschem* **2010,** *11* (9), 1854-7.

41. Desilvestro, J.; Weaver, M. J., *J. Electroanal. Chem.* **1986,** *209* (2), 377-386.
42. Liu, K.; Chen, T.; He, S.; Robbins, J. P.; Podkolzin, S. G.; Tian, F., *Angew. Chem. Int. Ed. Engl.* **2017,** *56* (42), 12952-12957.
43. Rossmeisl, J.; Logadottir, A.; Nørskov, J. K., *Chem. Phys.* **2005,** *319* (1-3), 178-184.
44. Kwon, Y.; Lai, S. C.; Rodriguez, P.; Koper, M. T., *J. Am. Chem. Soc.* **2011,** *133* (18), 6914-7.
45. Chen, X.; Aschaffenburg, D. J.; Cuk, T., *Nat. Catal.* **2019,** *2* (9), 820-827.
46. Koper, M. T. M., *Top. Catal.* **2015,** *58* (18-20), 1153-1158.
47. Kafizas, A.; Ma, Y.; Pastor, E.; Pendlebury, S. R.; Mesa, C.; Francàs, L.; Le Formal, F.; Noor, N.; Ling, M.; Sotelo-Vazquez, C.; Carmalt, C. J.; Parkin, I. P.; Durrant, J. R., *ACS Catal.* **2017,** *7* (7), 4896-4903.
48. Imanishi, A.; Okamura, T.; Ohashi, N.; Nakamura, R.; Nakato, Y., *J. Am. Chem. Soc.* **2007,** *129* (37), 11569-11578.